nature chemistry

ARTICLES

https://doi.org/10.1038/s41557-019-0332-8

Photodriven quantum teleportation of an electron spin state in a covalent donor–acceptor–radical system

Brandon K. Rugg, Matthew D. Krzyaniak, Brian T. Phelan, Mark A. Ratner, Ryan M. Young and Michael R. Wasielewski*

Quantum teleportation transfers the quantum state of a system over an arbitrary distance from one location to another through the agency of quantum entanglement. Because quantum teleportation is essential to many aspects of quantum information science, it is important to establish this phenomenon in molecular systems whose structures and properties can be tailored by synthesis. Here, we demonstrate electron spin state teleportation in an ensemble of covalent organic donor–acceptor–stable radical (D–A–R$^{\bullet}$) molecules. Following preparation of a specific electron spin state on R$^{\bullet}$ in a magnetic field using a microwave pulse, photoexcitation of A results in the formation of an entangled electron spin pair D$^{\bullet+}$–A$^{\bullet-}$. The spontaneous ultrafast chemical reaction D$^{\bullet+}$–A$^{\bullet-}$–R$^{\bullet}$ → D$^{\bullet+}$–A–R^{-} constitutes the Bell state measurement step necessary to carry out spin state teleportation. Quantum state tomography of the R$^{\bullet}$ and D$^{\bullet+}$ spin states using pulse electron paramagnetic resonance spectroscopy shows that the spin state of R$^{\bullet}$ is teleported to D$^{\bullet+}$ with high fidelity.

Quantum teleportation is a procedure that transfers a quantum state over an arbitrary distance from one location to another through the agency of quantum entanglement[1]. Measuring a quantum state in an attempt to copy it destroys the information it contains, leaving teleportation the only option for transmitting the state with high fidelity[2]. Several years after first being proposed in 1993[3], experimental evidence of quantum teleportation was obtained using photonic qubits[4,5]. Teleportation has since been observed for the states of various forms of matter, including trapped ions[6,7], atomic ensembles[8], superconducting circuits[9], nuclear spins[10], electron spins in quantum dots[11] and a combination of the electron and nuclear spins of nitrogen-vacancy centres in diamond[12]. However, demonstrations of this phenomenon in molecular systems amenable to tailoring by chemical synthesis, with its inherent advantages in constructing complex functional structures, have been notably absent. Here, we demonstrate electron spin state teleportation in an ensemble of covalent organic electron donor–acceptor–stable radical (D–A–R$^{\bullet}$) molecules using entangled electron spins produced by photoinduced electron transfer.

Preparing physical qubits in specific initial quantum states is essential for their use in quantum information science[13]. Subnanosecond photoinduced electron transfer in a structurally well-defined molecular donor–acceptor system can be used to produce an entangled spin qubit (radical) pair (RP) in a pure initial singlet state fulfilling this criterion. Photogenerated spin-entangled RPs occur in diverse molecular systems, including photosynthetic reaction centre proteins[14], electron donors and acceptors in micelles[15,16], covalent fixed-distance donor–acceptor molecules[17–19], cryptochromes implicated in the mechanism of the avian compass[20,21] and donor–acceptor systems that are part of DNA hairpin structures[22,23]. In many of these systems, multi-step electron transfer results in electron spin coherence being maintained over several nanometres for tens of microseconds, making it possible to synthesize and use complex molecular assemblies for quantum information applications. Recently, it has been recognized that spin-entangled RPs produced by ultrafast electron transfer can be used to implement two-qubit quantum information protocols[24–32], and to probe the nature of quantum measurement in molecular systems[33]. Importantly, Salikhov and others have proposed that a spontaneous electron transfer reaction from one of the radicals within a spin-entangled RP to a third radical bearing a prepared spin state, thereby reducing the radical to a diamagnetic anion, can serve as the Bell state measurement step necessary to carry out spin state teleportation to the remaining radical[24,25].

Results and discussion

To accomplish electron spin teleportation in a molecular system, we synthesized a D–A–R$^{\bullet}$ molecule (**1**, Fig. 1), which consists of a 2,2,6,6-tetramethylbenzo[1,2-*d*:4,5-*d*′]bis([1,3]dioxole) donor (D), a 4-aminonaphthalene-1,8-imide acceptor/chromophore (A) and a partially deuterated α,γ-bisdiphenylene-β-phenylallyl radical (R$^{\bullet}$), as detailed in Supplementary Section 1. The electron transfer dynamics of D–A–R$^{\bullet}$ in a butyronitrile (PrCN) glass at 85 K were measured using transient absorption (TA) spectroscopy following selective photoexcitation of A at λ_{ex} = 416 nm. The energetics of the electron transfer reactions are described in Supplementary Section 2, while the TA data and details on the kinetics fitting procedures are provided in Supplementary Section 3.

Selective photoexcitation of A to its lowest excited singlet state produces D–^{1*}A–R$^{\bullet}$, which undergoes electron transfer to form the three-spin state D$^{\bullet+}$–A$^{\bullet-}$–R$^{\bullet}$ with a rate constant of ~1×10^{11} s^{-1}. The spins localized on D$^{\bullet+}$ and A$^{\bullet-}$ are initially entangled in a singlet ($S = 0$) spin state, which is an essential requirement for spin state teleportation in D$^{\bullet+}$–A$^{\bullet-}$–R$^{\bullet}$. Before the energetically favourable ($\Delta G \approx -1.1$ eV) electron transfer reaction D$^{\bullet+}$–A$^{\bullet-}$–R$^{\bullet}$ → D$^{\bullet+}$–A–R^{-}, the spin–spin exchange interaction between A$^{\bullet-}$ and R$^{\bullet}$ projects

Department of Chemistry and Institute for Sustainability and Energy at Northwestern, Northwestern University, Evanston, IL, USA.
*e-mail: m-wasielewski@northwestern.edu

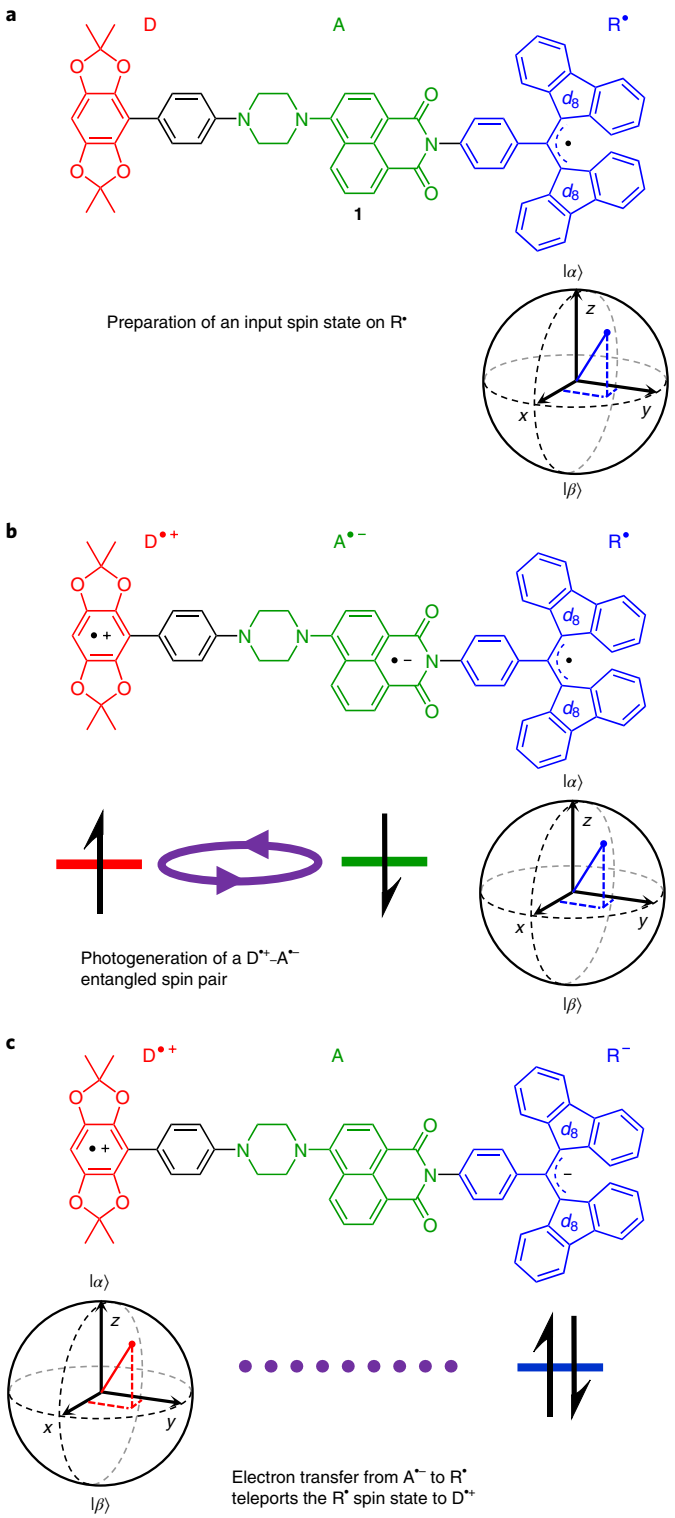

Fig. 1 | Electron spin state teleportation protocol. a, An arbitrary input state is prepared on R• with a resonant microwave pulse, which rotates the magnetization vector from its original position aligned along the $+z$ axis (direction of B_0). **b**, Photoexcitation of A results in ultrafast electron transfer from D to A, resulting in the formation of the D•+–A•− entangled spin pair in the presence of the prepared spin state on R•. **c**, Spin-selective electron transfer from A•− to R• constitutes a Bell state measurement that teleports the prepared state on R• to D•+.

these two spins randomly into the singlet–triplet basis of A•−–R•. This leads to a statistical population of 75% triplet D•+–^{3}(A•−–R•) and 25% singlet D•+–^{1}(A•−–R•) subensembles[34]. The Pauli exclusion principle requires that the reduction of R• to R− occurs only in the singlet subensemble, where the measured rate constant for the reaction D•+–^{1}(A•−–R•) → D•+–A–R− is ~1×10^{10} s^{-1}. The ^{1}(A•−-R•) singlet state, $|S\rangle = \frac{1}{\sqrt{2}}(|\uparrow\downarrow\rangle - |\downarrow\uparrow\rangle)$, is equivalent to one of the maximally entangled Bell states[35] and this process thus constitutes a partial Bell state measurement in which D•+ in the singlet subensemble acquires the original spin state of R•. By design, the charge recombination reaction D•+–A–R− → D–A–R• is slow, with a rate constant of 3×10^4 s^{-1}, while the charge recombination reaction of the triplet subensemble, D•+–^{3}(A•−–R•) → D–A–R•, occurs much more rapidly (~1×10^{10} s^{-1}). Thus, the D•+–A–R− subensemble, which is produced from the Bell state measurement with 25% efficiency, is the only species present on the >500 ns timescale of the EPR experiments described below, which allows for its selective detection.

EPR characterization. We employed a hierarchical series of pulse-EPR experiments to probe spin state teleportation in D–A–R•, beginning with single-frequency magnetic field swept, electron spin echo (FS-ESE) detection of D•+–A–R− to observe teleportation of the z-component $\langle S_z\rangle$ of the equilibrium magnetization of R• to D•+ relative to the amount of R• reduced. This permits estimation of the entanglement fidelity (F_{ent}) of D•+–A•−. Two-frequency transient nutation experiments were then used to confirm teleportation of $\langle S_z\rangle$, and determine the optimal microwave pulse lengths for preparing coherent states on R• and subsequently detecting the D•+ spin state. Finally, the teleportation protocol was tested with an unbiased sample of input states prepared on R•, using full quantum state tomography to quantify the fidelity of the electron spin states prepared on R• and subsequently teleported to D•+.

The steady-state EPR spectra of D•+ and R• shown in Fig. 2a were obtained using FS-ESE spectroscopy using a standard $\pi/2$–τ–π–τ–*echo* microwave pulse Hahn echo sequence (Supplementary Section 4), where in the rotating frame, the first $\pi/2$ pulse rotates the vector of the equilibrium magnetization aligned with the magnetic field (B_0) applied along the z axis into the x–y plane, forming a coherent superposition of the α and β spin states. Over time τ, the coherence of the ensemble dephases as the individual spins precess at slightly different rates due to inhomogeneities in their local magnetic environment. However, this inhomogenous dephasing is reversed by the application of the π pulse, which causes a detectable refocusing of the magnetization, that is, a spin echo, at τ after the pulse. The choice of D and R• is designed to ensure that the EPR spectra of D•+ and R• can be readily resolved. Thus, partial deuteration of R• results in a 0.26 mT linewidth, where its g factor is nearly isotropic (2.0026)[36], while D•+ has only a single proton hyperfine splitting and a mildly anisotropic g tensor, whose principal values are [2.0059, 2.00524, 2.00228]. This difference corresponds to a 40 MHz resonant frequency difference between the maxima of D•+ and R• in a 1.2 T magnetic field, which is sufficient to permit selective probing of each species.

The corresponding FS-ESE spectrum recorded 1 µs after photoexcitation of D–A–R• at 416 nm shows the appearance of a positive signal resulting from D•+ comparable to the negative (depleted) signal of R• (Fig. 2b). This result indicates that D•+ acquires a value of $\langle S_z\rangle$ very similar to that depleted from the R• ensemble because the $+z$ component of R• is teleported to D•+. Because the spin-lattice relaxation time of D•+ in PrCN at 85 K is $T_1 = 1.47 \pm 0.02$ ms (Supplementary Section 4), ⟨0.1% of the D•+ ensemble has relaxed at 1 µs following the formation of D•+–A–R−.

The spectrum in Fig. 2b also allows for a direct comparison of the resulting population of D•+ to the amount of R• depleted—information that we use to estimate F_{ent} of the initial photogenerated RP. Supplementary Section 4 describes the method used to obtain F_{ent}. Briefly, fitting the spectrum with area-normalized spec-

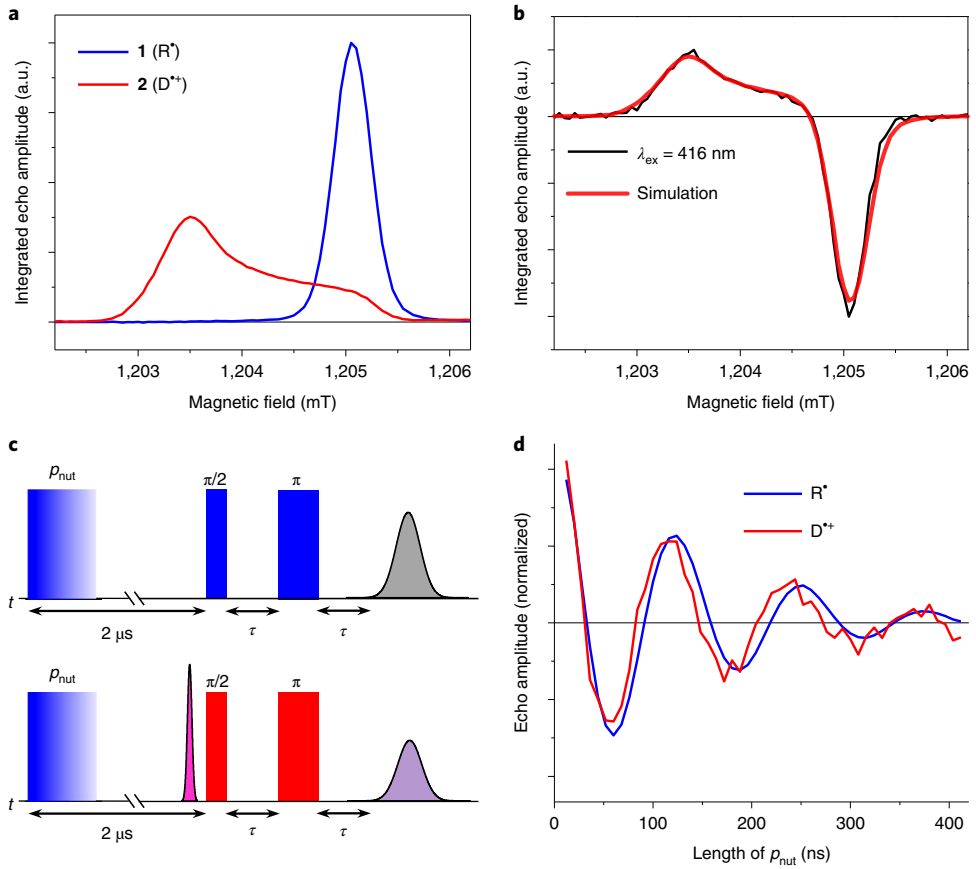

Fig. 2 | FS-ESE spectra and transient nutation data. a, FS-ESE spectra of R• and D•+ (area-normalized) obtained from compounds **1** and **2** (Supplementary Section 1). **b**, The FS-ESE spectrum of D•+–A–R⁻ after photoexcitation of D–A–R•. This spectrum was obtained with the laser pulse positioned 1 μs before the beginning of the $\pi/2$-τ-π-τ microwave pulse sequence, where the pulse lengths are $t_{(\pi/2)} = 40$ ns and $t_{(\pi)} = 80$ ns, while $\tau = 200$ ns. The simulation uses the normalized component spectra shown in **a** and provides an estimate of $F_{ent} = 0.91$. **c**, Pulse sequences used to detect the Rabi oscillations of R• (top) and photogenerated D•+ (bottom) induced by varying lengths of p_{nut}. The microwave pulses are colour-coded to the targeted spin, where pulses resonant with R• are shown in blue and those resonant with D•+ are in red, while the sharp magenta feature represents the laser pulse. The grey and purple peaks are electron spin echoes. **d**, The amplitudes of the detected echoes as a function of the length of p_{nut}. This demonstrates that the Rabi oscillations induced on R• are teleported to D•+ through the electron transfer reaction.

tra of R• and D•+ indicates the ratio of these two signals is 0.79. After correcting for the difference in phase memory times (T_m) of D•+ (0.89 ± 0.01 μs) and R• (1.16 ± 0.03 μs) and the length of the detection pulse sequence, we obtain $F_{ent} = 0.91$.

Teleportation of Rabi oscillations. The relationship between the spin population of D•+–A–R⁻ and the population of D–A–R• was further investigated using transient nutation experiments (Supplementary Section 4). First, a variable length nutation pulse, p_{nut}, was applied to R• within D–A–R•, generating a superposition of α and β states (Fig. 2c). Following p_{nut}, a Hahn echo detection sequence was performed to measure $\langle S_z \rangle$, and Rabi oscillations from R• were observed as a function of the length of p_{nut} (Fig. 2d). Next, p_{nut} was applied again to R•, the sample was photoexcited to produce D•+–A–R⁻ and finally the Hahn echo detection sequence was applied at a frequency resonant with D•+ (Fig. 2d). The echo amplitude of D•+ showed Rabi oscillations similar to those observed for R• in the experiment on D–A–R•, despite the fact that p_{nut} was applied to R• and occurred before D•+ was generated by photoexcitation (Fig. 2d). This experiment confirms that the reaction D•+–A•⁻–R• → D•+–A–R⁻ teleports $\langle S_z \rangle$ of R• to D•+.

Quantum teleportation and quantum state tomography. Although the two-frequency nutation experiment demonstrates that electron spin state $\langle S_z \rangle$ populations are teleported by the electron transfer reaction, a true quantum teleportation protocol is capable of transmitting any possible quantum state of the system—including coherent superposition states. This is typically verified by supplying an unbiased set of input states for testing, such as the six poles of the Bloch sphere. Following this precedent, we prepared these six states on R• using microwave pulses having specific phases and turning angles (Fig. 3 and Supplementary Fig. 6). Adequate preparation of the input states was ensured by performing quantum state tomography on R• following state preparation using two separate microwave pulse sequences: one to detect the spin echo resulting from $\langle S_z \rangle$ and another sequence to detect $\langle S_x \rangle$ and $\langle S_y \rangle$ as shown in Fig. 3 and Supplementary Fig. 6. Proper tuning of the detection phase ensured that signals due to $\langle S_z \rangle$ were observed only in the in-phase channel. $\langle S_x \rangle$ and $\langle S_y \rangle$ were detected in the in-phase and quadrature channels of the spectrometer, respectively. Next, the input states were again prepared in the same fashion with the preparation microwave pulse frequency resonant with R•, while the detection frequency was set 40 MHz higher to be resonant with D•+. The sample was then photoexcited ~7 ns after the microwave preparation pulse to initiate the two-step electron transfer sequence to produce D•+–A–R⁻, and the full quantum state tomography of D•+ was performed (Fig. 3 and Supplementary Fig. 6).

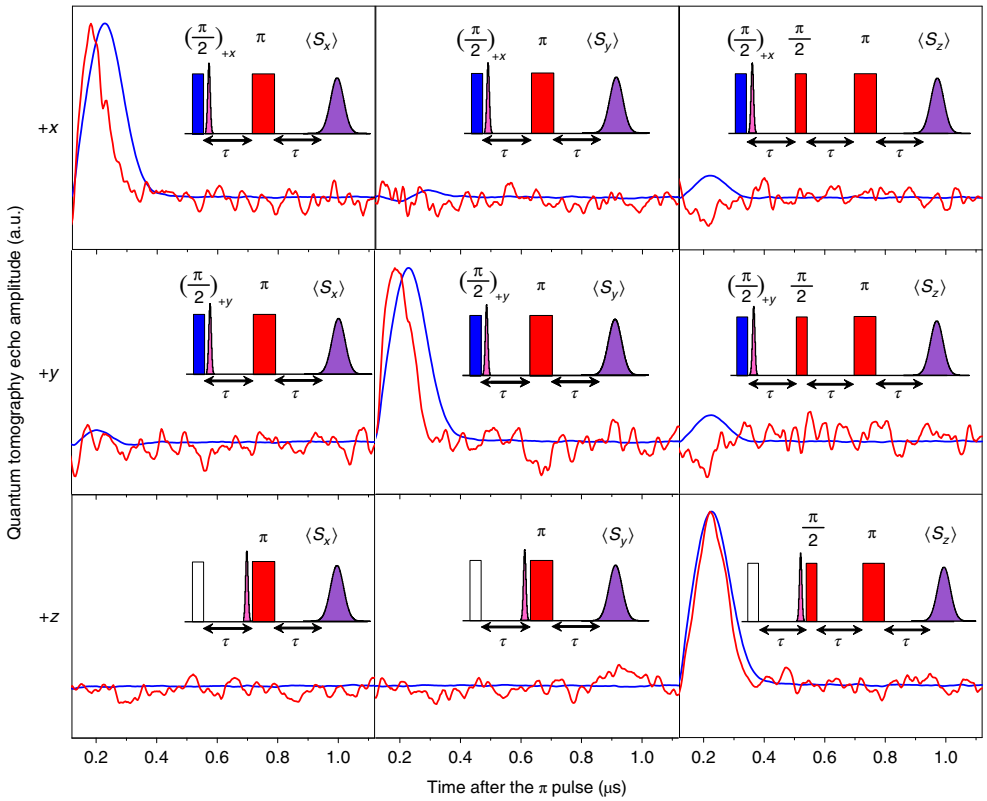

Fig. 3 | Quantum state tomography. The spin echoes, which represent the measurement of $\langle S_x \rangle$, $\langle S_y \rangle$ and $\langle S_z \rangle$ of a state prepared along the $+x$, $+y$ and $+z$ directions of the Bloch sphere using the pulse sequence shown in each panel. $\langle S_x \rangle$ and $\langle S_y \rangle$ are obtained from the spin echoes detected in the in-phase and quadrature channels of the EPR spectrometer, respectively. Microwave pulses resonant with R• are shown in blue, while those resonant with $D^{\bullet+}$ are shown in red. The laser pulse is the sharp magenta feature. The data obtained for the R• input state in the absence of the laser pulse (blue traces) are compared to those obtained for the teleported state on $D^{\bullet+}$ (red traces). The purple peaks are electron spin echoes. This demonstrates that the spin states initially prepared on R• have been teleported to $D^{\bullet+}$ with high fidelity. Note that tomography of the $+z$ component does not require the $\pi/2$ preparation pulse on R•.

Figure 3 shows the spin echoes obtained along the $+x$, $+y$ and $+z$ directions of the Bloch sphere that result from using the specific pulse sequences shown in each panel to give $\langle S_x \rangle$, $\langle S_y \rangle$ and $\langle S_z \rangle$. The corresponding data for the $-x$, $-y$ and $-z$ directions of the Bloch sphere are given in Supplementary Fig. 6. The data for the prepared spin state on R• (Fig. 3, blue traces) are obtained in the absence of the laser pulse, and indicate that $\langle S_x \rangle$, $\langle S_y \rangle$ and $\langle S_z \rangle$ are prepared with high fidelity (see below). For a given direction, $+x$, $+y$, or $+z$ of the Bloch sphere, the signals that appear in the other two directions are small or absent. In a separate experiment, microwave pulses resonant with R• again prepare its initial spin state, then a laser pulse creates $D^{\bullet+}$–A–R^{-}, and finally microwave readout pulses resonant with $D^{\bullet+}$ yield spin echoes that give $\langle S_x \rangle$, $\langle S_y \rangle$ and $\langle S_z \rangle$ (red traces). These spin echoes are comparable in magnitude to those obtained from the initially prepared electron spin state on R• in the absence of the laser pulse. Once again, the signals that appear in the other directions of the Bloch sphere are small or absent, showing that the spin state initially prepared on R• has been teleported to $D^{\bullet+}$ with high fidelity (see below).

The electron spin echoes observed for the states teleported to $D^{\bullet+}$ occur earlier than those of the prepared states of R• for $\langle S_x \rangle$ and $\langle S_y \rangle$. This results from the fact that the coherence generated by the state preparation pulse evolves under the Hamiltonian of R•, both during the microwave pulse and in the time before the electron transfer event that initiates teleportation. Following teleportation, the spin coherence continues to evolve under the Hamiltonian of $D^{\bullet+}$, is refocused with the π pulse, and the resulting spin echo obtains both a phase shift related to the 40 MHz frequency difference between R• and $D^{\bullet+}$ and a time shift due to the spin ensemble refocusing sooner under the Hamiltonian of $D^{\bullet+}$[37]. A similar phenomenon has been observed in previous demonstrations of quantum teleportation[12]. Another indication of the phase-coherent behaviour of the electron spin state teleported to $D^{\bullet+}$ is the observation that the x/y component of the state vector was observed to undergo a full phase rotation of 2π, while incrementally changing the time between the initial $\pi/2$ microwave pulse and the laser pulse over a period of 25 ns, that is, 1/(40 MHz) (Supplementary Fig. 7).

The results of the quantum state tomography experiments were used to calculate the density matrices of both the input states

Table 1 | Fidelity data: the microwave pulse used to prepare each input state and the corresponding fidelities of state preparation and teleportation.

State	Preparation pulse	F_{inp}	F_{tel}
$+x$	$(\pi/2)_{+x}$	0.99	0.89
$+y$	$(\pi/2)_{+y}$	0.99	0.89
$+z$	None	1.00	0.91
$-x$	$(\pi/2)_{-x}$	0.99	0.90
$-y$	$(\pi/2)_{-y}$	0.99	0.87
$-z$	$(\pi)_{+x}$	0.96	0.90
Avg.	-	0.99	0.89

prepared on R$^{\bullet}$ and the states teleported to D$^{\bullet+}$ (Supplementary Section 4). The trace of each density matrix was normalized to unity, which ignores the mixed character of ensemble spin states. We then used equation (1)[38], which allows a comparison of two density matrices ρ and σ, to calculate the teleportation fidelities of the input state on R$^{\bullet}$ (F_{inp}) and the teleported state (F_{tel}):

$$F(\rho,\sigma) \equiv \left(\mathrm{tr}\sqrt{\rho^{1/2}\sigma\rho^{1/2}}\right)^2 \quad (1)$$

Over the six states, an average value of $F_{inp}=0.99$ was obtained, which indicates a high fidelity of the prepared input states relative to the idealized target state (Table 1). We also obtained an average of $F_{tel}=0.89$, which is in large excess of the value of $F_{tel}>2/3$ necessary to confirm quantum teleportation[39].

Conclusions

The results presented here show that high-fidelity quantum teleportation of an electron spin state through the agency of a photogenerated entangled spin pair can be achieved in a covalent molecular assembly. We also establish the basic design criteria for expanding this approach to more complex molecular systems relevant to quantum information processing and manipulation.

Methods

Synthesis and optical spectroscopy. The synthesis and characterization of all compounds used in this study as well as their steady-state and transient optical spectroscopic data are presented in Supplementary Sections 1 and 3.

Instrumentation. All EPR experiments were performed on a laboratory-built Q-band (33.5 GHz, magnetic field $B_0=1.2$ T) spectrometer using a microwave bridge custom-built by Millitech/Smiths Interconnect. The microwave pulses were generated with a Keysight M8190A arbitrary waveform generator at an intermediate frequency between 0.5 and 2.5 GHz and upconverted to between 33.2 and 35.2 GHz in the microwave bridge; the signal was downconverted to baseband, detected in quadrature and digitized using an Agilent U1082A Acqiris card. The magnetic field was generated using a GMW model 3474–140 magnet and was controlled with a Lakeshore 475 DSP Gaussmeter. The temperature was maintained at 85 K using an Oxford Instruments CF935 Cryostat and an ITC503S temperature controller. The experiments were run with resonant frequencies around 33.5 GHz using a Bruker Q-Band EN 5107D2 resonator.

Signals were detected in both the in-phase (x) and quadrature (y) channels, with the phase manually adjusted to maximize the echo of R$^{\bullet}$ in the in-phase channel before detection. Two-frequency waveforms were calculated using the pulse function contained in EasySpin v5.2.10[40]. Unless indicated otherwise, the time between microwave pulses is $\tau=200$ ns. Echo amplitudes were calculated by integrating a region based on the full-width at half-maximum of the echo of R$^{\bullet}$ at resonance. Standard lengths for $\pi/2$ and π pulses were 40 and 80 ns, respectively, at the detection frequency. The pulse lengths at the secondary frequency targeting D$^{\bullet+}$ in the quantum tomography experiments were adjusted based on the outcome of the two-frequency nutation experiment (Supplementary Section 4). In the dataset shown in Fig. 2, lengths were adjusted to 38 and 76 ns for the $\pi/2$ and π pulses, respectively. The phase cycles used to obtain the data are provided in Supplementary Tables 1–3.

Sample preparation. Solutions of oxidized D-Ph-piperazine-Bn (compound **2**, Supplementary Section 1) were placed in a 10-cm-long (1.50 mm inner diameter (i.d.) and 1.80 mm outer diameter (o.d.)) quartz sample tube with a sample solution length of 2 cm, and subject to four freeze–pump–thaw cycles under vacuum (10^{-4} torr). These samples were flame-sealed and placed in the EPR resonator following typical procedures[23].

Samples for transient EPR studies were prepared by first measuring the optical density and volume of the solution of D–A–R$^{\bullet}$ in THF immediately after the radical generation process. The THF solution was evaporated to dryness under a stream of N_2. The samples were then reconstituted with a volume of PrCN (purged with N_2) calculated so that the resulting solution had an optical density of ~0.7 at $\lambda=416$ nm in a quartz cuvette with a 2 mm path length. This optical density corresponds to a concentration of ~0.25 mM. Quartz tubes 10 cm long (1.50 mm i.d. and 1.80 mm o.d.) were filled with an ~2 cm column of this sample solution. The tubes were then quickly fit with a length of optical fibre ~1.5 m long with a core diameter of 1 mm and numerical aperture of 0.39 (Thorlabs), which had been inserted through the Bruker sample holder rod, and positioned so that the tip of the fibre was slightly above the top of the sample solution. Before insertion of the fibre into the EPR tube, ~2 cm of the protective cladding was removed from the fibre to prevent any potential chemical interactions with the sample solution. The fibre and quartz tubes were sealed together using a short length of heat-shrink tubing; the tubing was positioned far enough away from the sample so that the sample was not heated during this process. The fibre was then coupled to an additional, longer optical fibre set up to receive 7 ns, 416 nm, 0.3 mJ pulses generated by an optical parametric oscillator (Spectra-Physics Basi-scan), pumped with the output of a frequency-tripled Nd:YAG laser (Spectra-Physics Quanta-Ray Lab 170) operating at a 10 Hz repetition rate.

Before insertion into the resonator, the sample was adjusted so that the top of the sample solution was positioned ~22 mm below the bottom of the sample-holding rod. The solution was then frozen by submersion in liquid N_2 and quickly inserted into the resonator, which had been pre-cooled to 85 K. This ensured that the PrCN would form a glass with little to no cracking to allow optimal photoexcitation. Once in the resonator, the sample height was adjusted by moving the sample-holding rod so that the resonant microwave frequency was 33.50 ± 0.5 GHz.

Data availability

The datasets generated and analysed in the current study are available from the corresponding author on reasonable request.

Received: 27 March 2019; Accepted: 13 August 2019;
Published online: 23 September 2019

References

1. Pirandola, S., Eisert, J., Weedbrook, C., Furusawa, A. & Braunstein, S. L. Advances in quantum teleportation. *Nature Photon.* **9**, 641–652 (2015).
2. Wootters, W. K. & Zurek, W. H. A single quantum cannot be cloned. *Nature* **299**, 802–803 (1982).
3. Bennett, C. H. et al. Teleporting an unknown quantum state via dual classical and Einstein–Podolsky–Rosen channels. *Phys. Rev. Lett.* **70**, 1895–1899 (1993).
4. Bouwmeester, D. et al. Experimental quantum teleportation. *Nature* **390**, 575–579 (1997).
5. Boschi, D., Branca, S., De Martini, F., Hardy, L. & Popescu, S. Experimental realization of teleporting an unknown pure quantum state via dual classical and Einstein–Podolsky–Rosen channels. *Phys. Rev. Lett.* **80**, 1121–1125 (1998).
6. Barrett, M. D. et al. Deterministic quantum teleportation of atomic qubits. *Nature* **429**, 737–739 (2004).
7. Riebe, M. et al. Deterministic quantum teleportation with atoms. *Nature* **429**, 734–737 (2004).
8. Sherson, J. F. et al. Quantum teleportation between light and matter. *Nature* **443**, 557–560 (2006).
9. Steffen, L. et al. Deterministic quantum teleportation with feed-forward in a solid state system. *Nature* **500**, 319–324 (2013).
10. Nielsen, M. A., Knill, E. & Laflamme, R. Complete quantum teleportation using nuclear magnetic resonance. *Nature* **396**, 52–55 (1998).
11. Gao, W. B. et al. Quantum teleportation from a propagating photon to a solid-state spin qubit. *Nat. Commun.* **4**, 2744 (2013).
12. Pfaff, W. et al. Unconditional quantum teleportation between distant solid-state quantum bits. *Science* **345**, 532–535 (2014).
13. DiVincenzo, D. P. The physical implementation of quantum computation. *Fortschritte der Physik* **48**, 771–783 (2000).
14. Thurnauer, M. C. & Norris, J. R. An electron spin echo phase shift observed in photosynthetic algae: possible evidence for dynamic radical pair interactions. *Chem. Phys. Lett.* **76**, 557–561 (1980).
15. Sakaguchi, Y., Hayashi, H., Murai, H. & I'Haya, Y. J. CIDEP study of the photochemical reactions of carbonyl compounds showing the external magnetic field effect in a micelle. *Chem. Phys. Lett.* **110**, 275–279 (1984).
16. Closs, G. L., Forbes, M. D. E. & Norris, J. R. Spin-polarized electron-paramagnetic resonance-spectra of radical pairs in micelles—observation of electron spin–spin interactions. *J. Phys. Chem.* **91**, 3592–3599 (1987).
17. Hasharoni, K. et al. Mimicry of the radical pair and triplet states in photosynthetic reaction centers with a synthetic model. *J. Am. Chem. Soc.* **117**, 8055–8056 (1995).
18. Carbonera, D. et al. EPR investigation of photoinduced radical pair formation and decay to a triplet state in a carotene–porphyrin–fullerene triad. *J. Am. Chem. Soc.* **120**, 4398–4405 (1998).
19. Kobori, Y. et al. Primary charge-recombination in an artificial photosynthetic reaction center. *Proc. Natl Acad. Sci. USA* **102**, 10017–10022 (2005).
20. Sheppard, D. M. W. et al. Millitesla magnetic field effects on the photocycle of an animal cryptochrome. *Sci. Rep.* **7**, 42228 (2017).
21. Rodgers, C. T. & Hore, P. J. Chemical magnetoreception in birds: the radical pair mechanism. *Proc. Natl Acad. Sci. USA* **106**, 353–360 (2008).
22. Carmieli, R., Thazhathveetil, A. K., Lewis, F. D. & Wasielewski, M. R. Photoselective DNA hairpin spin switches. *J. Am. Chem. Soc.* **135**, 10970–10973 (2013).

23. Olshansky, J. H., Krzyaniak, M. D., Young, R. M. & Wasielewski, M. R. Photogenerated spin-entangled qubit (radical) pairs in DNA hairpins: observation of spin delocalization and coherence. *J. Am. Chem. Soc.* **141**, 2152–2160 (2019).
24. Salikhov, K. M., Golbeck, J. H. & Stehlik, D. Quantum teleportation across a biological membrane by means of correlated spin pair dynamics in photosynthetic reaction centers. *Appl. Magn. Reson.* **31**, 237–252 (2007).
25. Kandrashkin, Y. E. & Salikhov, K. M. Numerical simulation of quantum teleportation across biological membrane in photosynthetic reaction centers. *Appl. Magn. Reson.* **37**, 549–566 (2010).
26. Volkov, M. Y. & Salikhov, K. M. Pulse protocols for quantum computing with electron spins as qubits. *Appl. Magn. Reson.* **41**, 145–154 (2011).
27. Miura, T. & Wasielewski, M. R. Manipulating photogenerated radical ion pair lifetimes in wire-like molecules using microwave pulses: molecular spintronic gates. *J. Am. Chem. Soc.* **133**, 2844–2847 (2011).
28. Kobr, L. et al. Fast photodriven electron spin coherence transfer: a quantum gate based on a spin exchange J-jump. *J. Am. Chem. Soc.* **134**, 12430–12433 (2012).
29. Krzyaniak, M. D. et al. Fast photo-driven electron spin coherence transfer: the effect of electron-nuclear hyperfine coupling on coherence dephasing. *J. Mater. Chem. C* **3**, 7962–7967 (2015).
30. Kelber, J. B. et al. Synthesis and investigation of donor–porphyrin–acceptor triads with long-lived photo-induced charge-separate states. *Chem. Sci.* **6**, 6468–6481 (2015).
31. Nelson, J. N. et al. Zero quantum coherence in a series of covalent spin-correlated radical pairs. *J. Phys. Chem. A* **121**, 2241–2252 (2017).
32. Nelson, J. N. et al. Effect of electron-nuclear hyperfine interactions on multiple-quantum coherences in photogenerated covalent radical (qubit) pairs. *J. Phys. Chem. A* **122**, 9392–9402 (2018).
33. Jones, J. A. & Hore, P. J. Spin-selective reactions of radical pairs act as quantum measurements. *Chem. Phys. Lett.* **488**, 90–93 (2010).
34. Rugg, B. K. et al. Spin-selective photoreduction of a stable radical within a covalent donor–acceptor–radical triad. *J. Am. Chem. Soc.* **139**, 15660–15663 (2017).
35. Bell, J. S. On the Einstein–Poldolsky–Rosen paradox. *Physics* **1**, 195–200 (1964).
36. Hamilton, W. O. & Pake, G. E. Linear antiferromagnetism in the organic free radical 1,3-bisdiphenylene-2-phenyl allyl. *J. Chem. Phys.* **39**, 2694–2697 (1963).
37. Schweiger, A. & Jeschke, G. *Principles of Pulse Electron Paramagnetic Resonance* 1st edn (Oxford Univ. Press, 2001).
38. Bao, X.-H. et al. Quantum teleportation between remote atomic-ensemble quantum memories. *Proc. Natl Acad. Sci. USA* **109**, 20347–20351 (2012).
39. Grosshans, F. & Grangier, P. Quantum cloning and teleportation criteria for continuous quantum variables. *Phys. Rev. A* **64**, 010301 (2001).
40. Stoll, S. & Schweiger, A. EasySpin, a comprehensive software package for spectral simulation and analysis in EPR. *J. Magn. Reson.* **178**, 42–55 (2006).

Acknowledgements

This work was supported by the US National Science Foundation under grant no. CHE-1565925.

Author contributions

M.R.W. conceived of the project. B.K.R. synthesized the molecules, performed EPR experiments and analysed the data. B.T.P. performed the transient optical spectroscopy and B.K.R. analysed the results with input from B.T.P., R.M.Y. and M.R.W. M.D.K. designed and implemented AWG upgrades to the Q-band EPR spectrometer, obtained EPR data and, along with B.K.R. and M.R.W., analysed the data. M.A.R. provided theory input for data analysis. B.K.R., M.D.K. and M.R.W. wrote the manuscript with input and edits from all authors.

Competing interests

The authors declare no competing interests.

Additional information

Supplementary information is available for this paper at https://doi.org/10.1038/s41557-019-0332-8.

Reprints and permissions information is available at www.nature.com/reprints.

Correspondence and requests for materials should be addressed to M.R.W.

Publisher's note Springer Nature remains neutral with regard to jurisdictional claims in published maps and institutional affiliations.